Article

Not peer-reviewed version

Enhancing the Selective Reduction of Nickel to Prepare FeNi50 Alloy from Saprolite-Type Laterite by CO-CO_2 Gas Pretreatment

Zhichao Hu , Zhengliang Xue * , Guihua Hang , Guo Lin , Wei Wang , Fang Huang , Yaqi Wang

Posted Date: 17 December 2025

doi: 10.20944/preprints202512.1573.v1

Keywords: saprolite-type laterite; iron homogenization; selective nickel reduction; selective oxidation; FeNi50 alloy

Article

Enhancing the Selective Reduction of Nickel to Prepare FeNi50 Alloy from Saprolite-Type Laterite by CO-CO_2 Gas Pretreatment

Zhichao Hu [1], Zhengliang Xue [1,*], Guihua Hang [2], Guo Lin [3], Wei Wang [1], Fang Huang [1] and Yaqi Wang [1]

[1] State Key Laboratory of Refractories and Metallurgy, Wuhan University of Science and Technology, Wuhan 430081, China

[2] Automotive institute, Hubei communications technical college, Wuhan 430202, China

[3] School of Metallurgical and Energy Engineering, Kunming University of Science and Technology, Kunming, Yunnan 650093, China

* Correspondence: xuezhengliang@wust.edu.cn

Abstract

Owing to the superior reduction kinetics of limonite and goethite relative to silicates, coupled with the poor beneficiation performance of saprolite-type laterite, the direct carbothermal reduction of saprolite-type laterite exhibits limited nickel selectivity. This study leverages the selective oxidation effect of CO-CO2 atmosphere on metallic iron and its suppression of Fe2+ reduction to promote iron migration from oxides into the silicate phase, achieving homogenization and thereby negating its kinetic advantage in reduction. Parameter optimization experiments revealed that treating pre-reduced minerals with a 30 vol% CO atmosphere at 1200 °C for 20 minutes achieves complete iron homogenization within the silicate phase. Compared with the nickel-iron alloy (containing less than 10 wt% Ni) obtained via RKEF process, the combination of pre-reduction, CO-CO2 treatment, and melting reduction process yielded nickel-iron alloys with nickel contents of 52.1 wt% (FeNi50 alloy) and 64.2 wt% at carbon consumptions of 4.0 wt% and 3.83 wt%, respectively, accompanied by nickel recovery rates of 95.5% and 91.2%. Furthermore, the enrichment of Fe2+ in the slag significantly reduces its melting point to approximately 1450 °C, enabling complete slag-metal separation after smelting at 1550 °C for 10 minutes.

Keywords: saprolite-type laterite; iron homogenization; selective nickel reduction; selective oxidation; FeNi50 alloy

---

1. Introduction

Nickel exhibits excellent chemical and physical properties, rendering it extensively utilized in diverse applications including high-strength steel, stainless steel, high-temperature alloys, catalysts, and battery technologies [1–6]. As a high-demand element, global nickel production attained 3.7 million metric tons in 2024 [7]. Given the limited discovery of new nickel sulfide deposits in recent years, approximately 70% of current nickel production is extracted from laterite nickel ores, with this proportion demonstrating a consistent upward trend [8].

Laterite nickel ores represent the weathering profile of ultramafic protolith [9,10]. In tropical and subtropical regions with an annual precipitation exceeding 1,000 mm, the dissolution of silicon, magnesium, and partial nickel from the protolith into groundwater occurs, while residual iron oxides accumulate on the surface, forming limonitic laterite nickel ores [11]. At the groundwater table interface, nickel combines with silicon and magnesium to generate hydrated silicates, accompanied by limonite and protolith residues, thereby constituting saprolite-type lateritic nickel ores [12,13]. Limonitic laterite nickel ores, characterized by their high iron content, are predominantly utilized in

doi:10.20944/preprints202512.1573.v1

blast furnaces for low-nickel-content pig iron production or manufacturing pure nickel and cobalt through hydrometallurgical process. Saprolite-type laterite nickel ores are mainly processed by pyrometallurgical process to produce iron-nickel alloy.

Recent research endeavors in hydrometallurgical process have primarily concentrated enhancing the leaching efficiency of nickel, elevating the recovery rate of nickel, and, most critically, mitigating the environmental pollution. For instance, several technics have demonstrated the stress induced by techniques including roasting or microwave at a temperature of 600-800 °C for 1-2 hours irradiation can effectively disrupt mineral structures, consequently enhancing nickel leaching efficiency by a factor of 2-4 [14–17]. The incorporation of surfactants of 2×10^{-5} mol/L of sodium dodecylbenzene sulfonate has been demonstrated to elevate the recovery of nickel from 85.2% to 99.6% [18,19] and mechanical agitation of 300 r/min [20–22] is wildly applied to mitigate nickel losses during the neutralization process by more than 90%. In the aspect of environmental protection, the organic acid leaching process was initially favored by researchers owing to its minimal environmental impact. Although recent research findings indicate that the leaching efficiency of organic acids like citric acid and oxalic acid falls short of meeting industrial production requirements [23–25], amidst the prevailing environmental protection initiatives, this technology demonstrates considerable potential for future development. Moreover, the organic solvents have been proved to leverage the mass-to-charge ratio disparity of ions to selectively leach nickel to reduce acid consumption [26]; the alkaline leaching process has also been demonstrated the similar leaching efficiency as acid leaching process does [14,27].

The conventional pyrometallurgical approach like Rotary Kiln Electric Furnace (RKEF) process, Blast Furnace, Direct Reduction Magnetic Separation (DRMS) lacks the selective nickel enrichment capability inherent in hydrometallurgical processes [28,29], however, can provide metallic nickel to steel and alloy industries, which account for 70% of global nickel consumption, with lower cost. For instance, the Rotary Kiln Electric Furnace (RKEF) process, which accounts for approximately 80% of laterite nickel ore consumption, provides metallic nickel with 200$ lower per ton. Nevertheless, due to the physical beneficiation method demonstrating limited effectiveness in enhancing the Ni/Fe ratio of raw materials [30], RKEF process is predominantly employed for smelting saprolite-type laterite nickel ores characterized by a nickel content exceeding 1.6 wt%, a SiO_2/MgO ratio ranging from 1.6 to 1.9, and an Fe/Ni ratio below 10. Since there fewer and fewer high nickel grade minerals, the majority nickel-iron alloy product contain nickel ranging from 8 wt% to 12 wt% [31,32], insufficient to directly produce some steel and alloy by their own. The nickel content of nickel matte produced via sulfide reduction roasting oxygen-enriched blowing process is comparable to that achieved through hydrometallurgical methods. However, the elevated production costs associated with the sulfidation stage, coupled with a relatively low nickel recovery rate (approximately 80%), render this approach also economically comparable to hydrometallurgical methods [31].

In stainless steel production, every 1% increase in the nickel content within nickel iron extracted form laterite reduces stainless steel smelting costs by 50 $/t [31]. In order to enhance the selective reduction of nickel, some research have applied sulfides or sulfates to convert FeO into FeS, thereby inhibiting iron metallization process and elevating nickel grade of alloy by a factor of 1.5-3 [33–36]. Nevertheless, the associated costs of additives and nickel loss during the sulfidation process constrain its industrial application. Hydrogen plasma can heat mineral rapidly to its melting point within 5 min, which significantly mitigates the kinetic reduction advantage of oxides. However, as reported by U. Manzoor et al. [37] the selective reduction capability of hydrogen plasma towards nickel failed to attain the theoretically anticipated value to yield high-grade ferronickel (70-90 wt% Ni content) with corresponding total recovery rates ranging from 60 % to 90%. After multiple reduction steps the nickel content of alloy decreased to 30 wt%, with a nickel recovery rate of 78%. It must be noticed that under non-molten reduction conditions, the reduction rate of limonite (the predominant iron-bearing phase in lateritic nickel ores) substantially exceeds that of silicate (the principal nickel-bearing phase in lateritic nickel ores) [28]. Given that the reduction process commences prior to the mineral's melting phase, the actual reduction mechanism of laterite nickel ore inevitably deviates from the theoretically predicted homogeneous phase. As indicated by some research, the enhanced sintering process of iron with silicate induced by adding fluxes such as CaO, CaF_2, and NaCl deteriorates the reduction mechanism of iron of oxide, thus enhancing the selective reduction of nickel [28,38,39]. Nevertheless, these approaches present insufficient transformation of iron oxide, yield alloy of nickel concentration less than 20%.

Notably, CO-CO_2 mixed gas system exhibits remarkable performance in restraining the reduction of Fe^{2+}, which has been demonstrated efficacy in refining low-nickel grade laterite [40,41]. From the perspective of mineral phase, the application of CO-CO_2 mixed gas (which could obtain from the tail gas of pyrometallurgical process) presents potential to completely transform iron oxide into iron silicate, which eliminates the reduction priority of iron oxides, without additional additive. This study aims to elucidate the homogenization process of iron within the mineral under a CO-CO_2 atmosphere, and how this process facilitates the subsequent selective nickel reduction in smelting process to extract FeNi50 alloy from low-nickel grade saprolite-type laterite ore.

2. Materials and Methods

2.1. Material

The raw material of this research involves saprolite-type lateritic nickel ore from Sulawesi Island, Indonesia, and anthracite from Shanxi China. Table 1 presents the chemical analysis of the dried materials (desiccated at 120 °C until reaching constant weight). The quantification of non-oxygen elements was conducted through ICP-AES and XRF, while Fe^{2+} content was ascertained via titration method. The mineral represents a low-grade saprolite-type lateritic nickel ore, characterized by a SiO_2/MgO molar ratio of 2.9 and a Fe/Ni mass ratio of 11.3 (Figure 1a). The industrial production data pertaining to this mineral demonstrates that, without refining treatment, the RKEF process could only yield nickel-iron alloys with a nickel content below 10 wt%. The desiccated anthracite exhibited a fixed carbon content of 69.92 wt% (Table 2). The occurrence states of iron and nickel in the mineral were determined through chemical phase analysis [42], with the corresponding results presented in Table 3.

Table 1. Composition of saprolite-type laterite nickel ore (wt%).

Fe^{3+}	Fe^{2+}	T.Ni	SiO_2	MgO	Al_2O_3	CaO	T.Cr	T.Mn	T.Co	IL
15.89	0.56	1.46	42.06	15.23	2.73	0.79	0.88	0.35	0.045	14.33

Table 2. Occurrence states of Ni and Fe in saprolite-type laterite nickel ore (%).

Distribution	Sulfides	Oxides	Silicates	Manganese
Ni	0.4	19.3	79.3	1.0
Fe	0.8	61.1	37.7	0.4

Table 3. Composition of anthracite (wt%).

C	Ca	Mg	Si	Al	Fe	Volatiles
69.92	1.75	0.79	5.71	0.97	1.82	8.75

The analytical data indicates that nickel and iron predominantly exist in oxide and silicate forms, respectively, wherein approximately 80% of nickel is present in silicates and about 60% of iron is found in oxides. The phase analysis and elemental distribution of the mineral were characterized by XRD and SEM-EDS, as illustrated in Figure 1a,c. Mineralogical analysis revealed that the specimen predominantly consists of quartz, limonite, and silicate phases. Due to the isomorphic occurrence state of nickel with iron within oxides and iron and magnesium within silicates [28,40], no discrete nickel-rich mineral phases was observed. Given the complex phase assemblage of the specimen and the intensive picks of all characteristic XRD peaks concentrate within the 10° to 60° 2θ range, the XRD analysis presented in this study is confined to this angular range to facilitate clearer interpretation and comparison. The TG-DSC curves of the minerals are presented in Figure 1b. Owing to capillary action, the adsorbed water is released at 113 °C. The dehydration of goethite occurs at 315 °C, while that of silicate takes place at approximately 636 °C. The endothermic peak observed at 818 °C corresponds to the recrystallization process of certain silicate minerals.

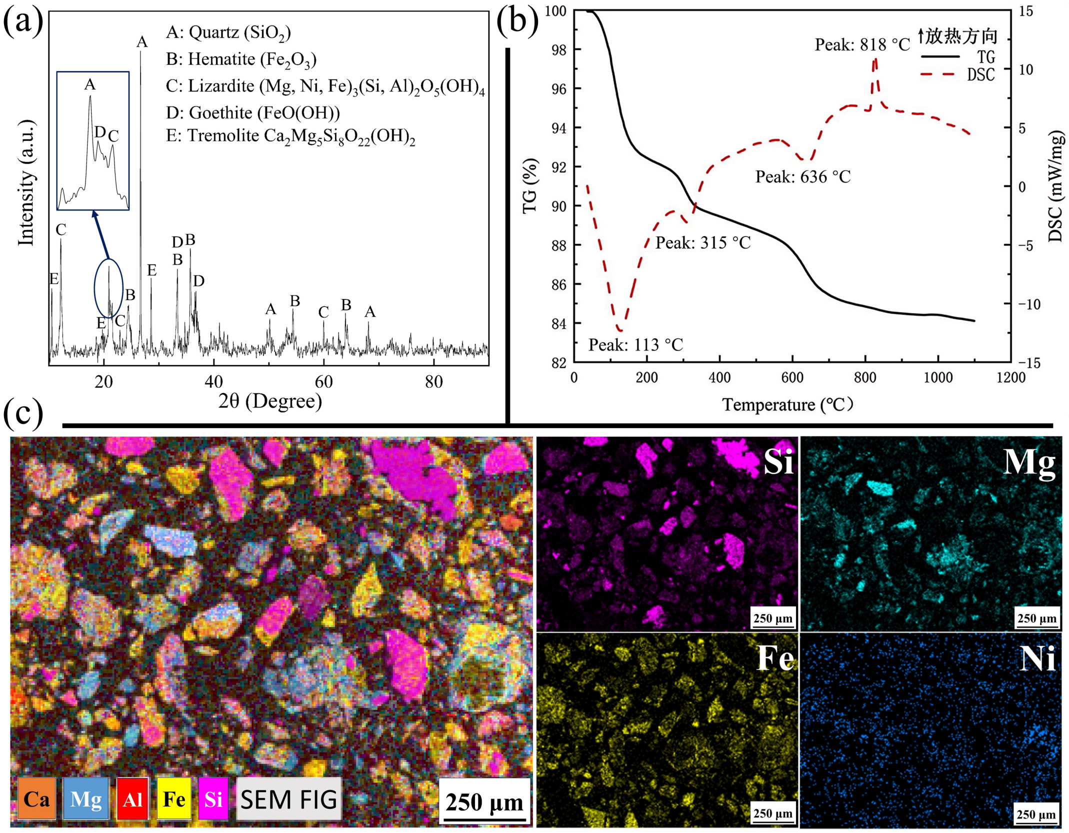

Figure 1. Material analysis: (a) XRD analysis of saprolite-type laterite nickel ore; (b) TG-DSC analysis of saprolite-type laterite nickel ore; (c) SEM-EDS analysis of saprolite-type laterite nickel ore.

2.2. Method

Specimen Preparation Procedure: The dried ore and anthracite were pulverized to a particle size of less than 18 mesh and homogenously blended at a mass ratio of 100:9.5. Subsequently, the mixture was compacted into cylindrical specimens with a diameter of 20 mm at a pressure of 10 MPa. The prepared specimens exhibited a carbon content of 6.1 wt%, with a molar ratio of fixed carbon to oxygen in iron oxides and nickel oxide of 1.2:1.

Pre-reduction-oxidation procedure: The specimen (300g ± 0.1g per batch) is positioned within a nickel-chromium alloy basket and subjected to thermal treatment in an alumina tube furnace, which is subsequently heated at a rate of 30 °C/min until reaching the designated reduction temperature. Throughout the Reduction phase, ultra-high-purity nitrogen gas (99.999%) is introduced into the tube furnace. Upon completion of the pre-reduction, the tube furnace temperature is adjusted to the oxidation temperature at a rate of 50 °C/min, during which the ultra-high-purity nitrogen gas is replaced with an oxidizing gas mixture for isothermal oxidation. Following the oxidation, the oxidizing gas is switched back to ultra-high-purity nitrogen gas, and the specimen is furnace-cooled to ambient temperature prior to removal.

Smelting procedure: The smelting specimens are positioned within an alumina crucible and subjected to smelting in a carbon tube furnace. The furnace is heated at a controlled rate of 100 °C/min until reaching 1600 °C, maintaining this temperature for a duration of 10 minutes. Subsequently, the specimen is furnace-cooled to ambient temperature, after which they are extracted for subsequent slag-metal separation. Throughout the entire process, a continuous flow of high-purity nitrogen is maintained.

For each specimen, four independent component analyses were performed, and the median value of the intermediate two measurements was adopted as the analytical result. Specifically, the determination of metallic iron and nickel in the pre-reduction and oxidized specimens was conducted through the alkali eutectic and ferric chloride leaching methodology [43]. The metallization degree of nickel (MNi) and iron (MFe) of pre-reduced specimens and oxidized specimens are determined by Equations (1) and (2), respectively:

$$\mathrm{MNi} = (w_s(\mathrm{MNi}) / w_s(\mathrm{TNi})) \times 100\% \tag{1}$$

$$\mathrm{MFe} = (w_s(\mathrm{MFe}) / w_s(\mathrm{TFe})) \times 100\% \tag{2}$$

where ws(TNi) and ws(TFe) denote the mass fractions of total nickel and total iron within specimens, while ws(MNi) and ws(MFe) represent the mass fractions of metallic nickel and metallic iron within specimens, respectively. The oxidation degree of nickel (ONi), iron (OFe) and carbon (OC) are determined by Equations (3) to (5), respectively:

$$O_{\mathrm{Ni}} = ((\mathrm{MNiR} - \mathrm{MNiO}) / \mathrm{MNiR}) \times 100\% \tag{3}$$

$$O_{\mathrm{Fe}} = ((\mathrm{MFeR} - \mathrm{MFeO}) / \mathrm{MFeR}) \times 100\% \tag{4}$$

$$O_{\mathrm{C}} = \left(\left(\frac{w_R(\mathrm{C})}{w_R(\mathrm{Mg})} - \frac{w_O(\mathrm{C})}{w_O(\mathrm{Mg})}\right) / \frac{w_R(\mathrm{C})}{w_R(\mathrm{Mg})}\right) \times 100\% \tag{5}$$

where MNiO and MFeO refer to the metallization degree of nickel and iron within oxidized specimens; MNiR and MFeR denote the metallization degree of nickel and iron within pre-reduced specimens; wR(C) and wO(C) represent the mass fractions of carbon in pre-reduced specimens and oxidized specimens; wR(Mg) and wO(Mg) represent the mass fractions of magnesium in pre-reduced specimens and oxidized specimens, respectively. The recovery rate of nickel (RNi) and iron (RFe) are calculated using Equations (6) and (7), respectively:

$$R_{\mathrm{Ni}} = (w_a(\mathrm{Ni}) \times m_a) / (w_{sl}(\mathrm{Ni}) \times m_{sl} + w_a(\mathrm{Ni}) \times m_a) \times 100\% \tag{6}$$

$$R_{\mathrm{Fe}} = (w_a(\mathrm{Fe}) \times m_a) / (w_{sl}(\mathrm{Fe}) \times m_{sl} + w_a(\mathrm{Fe}) \times m_a) \times 100\% \tag{7}$$

where wsl(Ni) and wsl(Fe) represent the mass fractions of nickel and iron for slag; wa(Ni) and wa(Fe) refer to the mass fractions of nickel and iron for alloy; ma and msl denote the mass of alloy and slag, respectively.

Other key parameters in this study encompass the relative nickel content in the alloy, denoted as C(Ni) (expressed as the mass percentage of Ni/(Ni+Fe)), the relative iron content in the alloy, designated as C(Fe) (represented as the mass percentage of Fe/(Ni+Fe)), the volumetric concentration of CO in the oxidizing atmosphere, φ(CO), and the volumetric concentration of CO_2 in the oxidizing atmosphere, φ(CO_2).

3. Results and Discussion

3.1. Carbothermic Reduction

Before elaborating on the CO-CO_2 treatment, it is essential to observe the carbothermal reduction of this mineral, particularly the kinetic constraints that impede nickel reduction. Mineral subjected to thermal treatment at 1000 °C is designated as the control group for comparative analysis. As depicted in Figure 2b, all goethite undergoes complete transformation into limonite, while most silicate hydrate transitions to an amorphous state due to the removal of crystalline water. Furthermore, given that the iron and nickel present in sulfides and manganese ores constitute approximately 1% of the total iron and nickel content, and considering the challenges in tracking the reduction process of these minerals along with their negligible impact on the overall reduction process of iron and nickel, this study primarily focuses on the reduction process of iron and nickel contained within oxides and silicates. To facilitate the differentiation of iron and nickel in various states of existence, the iron and nickel in oxides are designated as Fe(O) and Ni(O), respectively, while those in silicates are denoted as Fe(Si) and Ni(Si) in subsequent discussions.

The inherited physical difference between oxides and silicates lead to significant discrepancies in their reduction rates. The oxides exhibit a loose and porous structure, with their porosity further enhanced following dehydration. The substantial specific surface area facilitates comprehensive adsorption and diffusion of the reducing agent on its surfaces, thereby enabling their rapid reduction [44,45]. Silicates not only exhibit a dense crystalline structure, but also demonstrate a propensity for facile solid-state reactions with Fe^{2+} generated during the reduction process, which further impairs the reduction kinetics [41]. Given that approximately 20% of Ni and 60% of Fe in the specimens are present in oxide forms, it is reasonable to observe a significant decline in the metallization rate of Ni and Fe once Ni(O) and Fe(O) complete their reduction, as evidenced by the inflection points in the M_{Ni} and M_{Fe} curves when M_{Ni} and M_{Fe} reach 20% and 60%, respectively (Figure 2a).

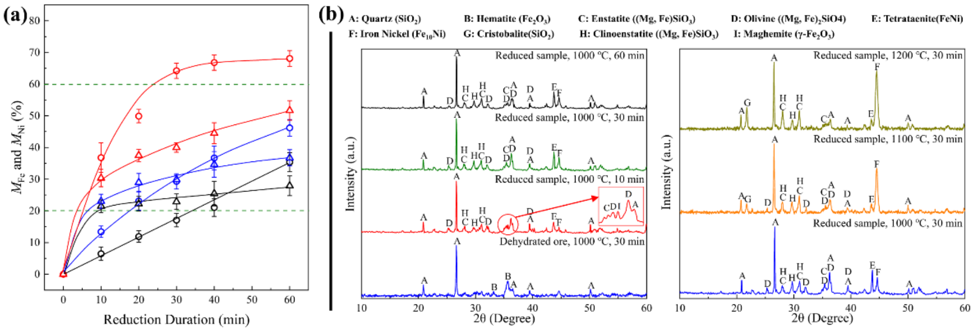

Figure 2. (a) M_{Fe} and M_{Ni} of reduced specimens; (b) XRD analysis of reduced specimens.

As illustrated in Figure 2b, the metallization of Ni and Fe of initial stage of the reduction process the is predominantly governed by the reduction of oxides: the predominant proportion of oxides has been reduced within 10 min at 1000 °C. Within this stage, the transformation of Fe(Si) into Fe^{2+} catalyzed the crystallization of amorphous silicates, resulting in the formation of enstatite and clinoenstatite. Concurrently, Ni(O) is directly reduced to metallic nickel, while the predominant portion of Fe(O) is reduced to Fe^{2+} and subsequently adsorbed into silicates to form an iron-rich olivine crust enveloping the silicate matrix (Figure 3a). This phenomenon elucidates the significantly impeded reduction kinetics of Fe(O), resulting in the metallization process of Fe(O) lagging the reduction process of oxides. Consequently, within the specimen reduced at 1000 °C for 10 min, M_{Ni} attains 21.5%, whereas M_{Fe} reaches only 6.9% (Figure 2a); the alloy product primarily consists of tetrataenite (with a nickel content ranging from 27 wt% to 65 wt%) (Figure 2b).

Nevertheless, the olivine crust formed the initial stage of the reduction exhibits a markedly larger specific surface area and preferentially initiates contact with the reducing agent compared to silicate matrix, thereby presenting substantially superior reduction kinetics. As depicted in Figure 2a, following the complete reduction of oxides, the metallization rate of nickel undergoes a notable deceleration (the inflection point of M_{Ni} curve), whereas iron maintains a relatively high metallization rate. As the reduction proceeds, both the increase of temperature and duration, the metallization rate of iron significantly increases and subsequently exceeding and diverging from that of nickel until the complete reduction of olivine, where the inflection of M_{Fe} curve is observed. From the microscopic perspective and XRD analysis, as depicted in Figures 2b and 3b, the olivine experiences a markedly faster reduction than the silicate matrix: as the reduction temperatures elevated, olivine progressively transfers into metallic iron (wherein tetrataenite assimilates metallic iron and transforms into an iron-nickel alloy), cristobalite, and enstatite, while little change in clinoenstatite content is observed. In the specimen reduced at 1200 °C for 30 min, olivine completes its reduction, leaving a metal-silicate transition layer with an approximate thickness of 3μm (Figure 3a). Concurrently, M_{Fe} and M_{Ni} achieve 64.2% and 40% respectively.

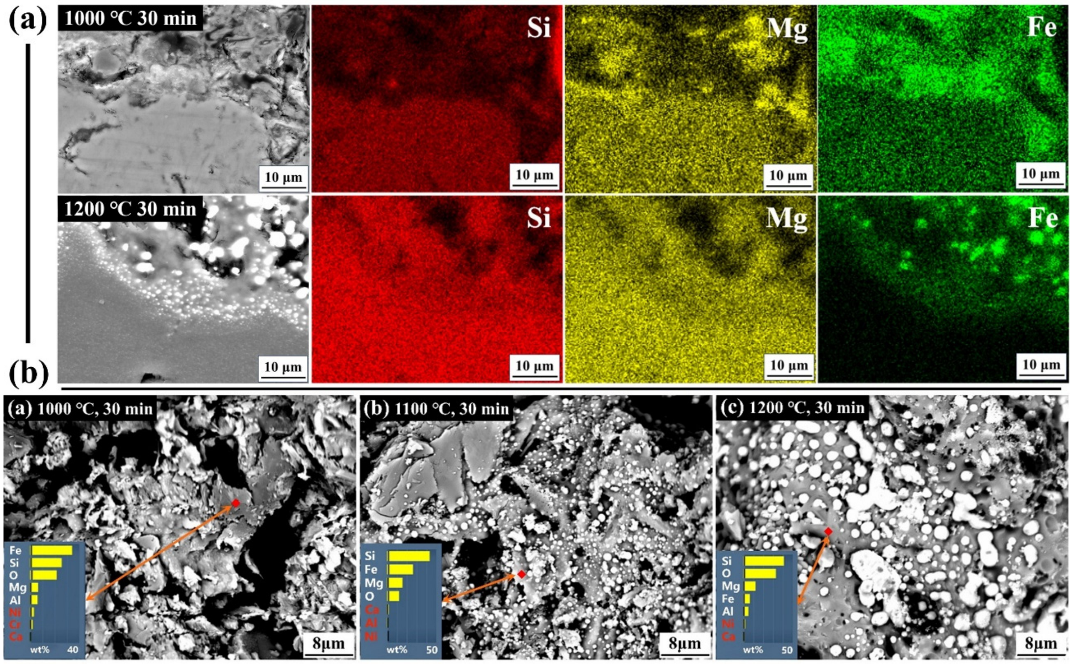

Figure 3. (a) SEM-EDS analysis of the cross-section surface; (b) SEM-EDS analysis of the fracture surface.

It is evident that the differential occurrence states of iron and nickel in mineral structures impose significant constraints on the reduction kinetics of nickel in non-molten reduction. Although mineral homogenization occurs post-melting, achieving uniform dispersion of the reductant within the molten mineral prior to triggering the reduction process presents significant challenges. Direct introduction of the reducing agent onto the melt surface will confine the reduction reaction to the interfacial region where the melt and reducing agent interact. When the reduction rate of Ni^{2+} surrounds the reductant exceeds the rate Ni^{2+} diffusing from the melting into the interfacial zone, the reduction rate of nickel decreases. Following the application of 4 wt% carbon powder onto the molten mineral surface at 1600 °C with a 10-minute holding period, the recovery rate of Ni (R_{Ni}) and Fe (R_{Fe}) were measured at 56.5% and 35.1%, respectively, indicating that the reduction advantage of nickel remains unremarkable.

In conclusion, at least two fundamental prerequisites are essential for achieving selective nickel reduction in minerals: complete homogenization of iron within the mineral matrix and uniform distribution of the reducing agent throughout the mineral.

3.2. CO-CO_2 Treatment

The oxidative potential of a CO_2-CO mixed gas exhibits significant variations in its interaction with metallic iron and metallic nickel. As depicted in Figure 4a (calculated using Factsage 8.2; Database: FactPs; Input parameters: molar ratio, temperature range 300-1300 °C, 1 atm), within the temperature range of 700 °C to 1300 °C, the oxidation resistance hierarchy follows the sequence: $Ni > Fe_3O_4 > FeO > Fe > C$. In an oxidation temperature of 1200 °C, to achieve complete inhibition of metallic iron oxidation, the volume fraction of CO (φ(CO)) must exceed 77.8%, whereas for complete inhibition of metallic nickel oxidation, a φ(CO) value above 2.4% is sufficient. This computation result shows an alignment with the experimental findings reported by Hang et al. a gas mixture containing 70% CO ($\varphi(CO) = 70\%$) failed to reduce Fe^{2+} in saprolite-type laterite nickel ore to metallic iron at a temperature of 1100 °C [38]. Consequently, from a thermochemical perspective, the application of this gas mixture can facilitate the Fe^{2+} diffusion into the silicate matrix interior, thereby achieving iron homogenization within the silicate matrix.

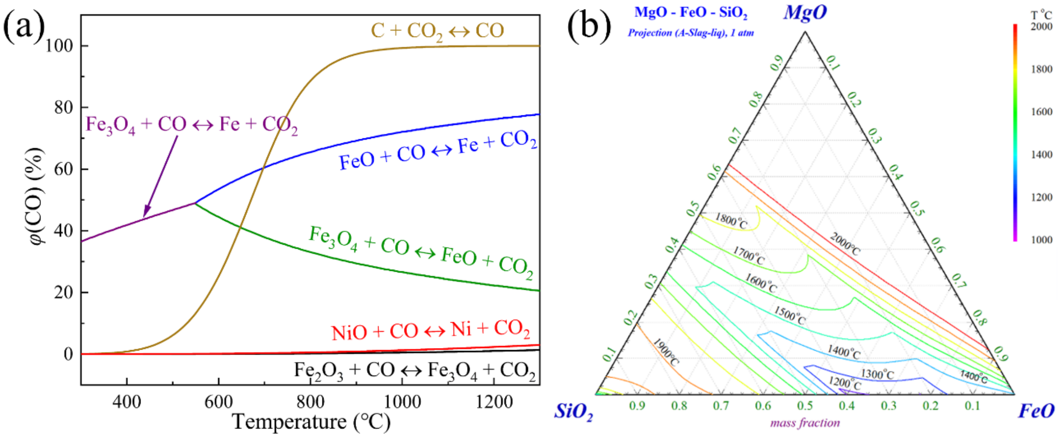

Figure 4. Phase equilibrium diagram. (a) equilibrium phase diagrams of iron, nickel, carbon, and their corresponding oxides in CO-CO$_2$ mixed gas atmospheres; (b) melting point of SiO$_2$-FeO-MgO slag.

A pure CO$_2$ with a controlled flow rate of 2 L/min was employed to oxidize the pre-reduced specimens (which were pre-reduced at 1200 °C for 30 minutes) to observe the behavior of iron, nickel, and carbon in CO$_2$ atmosphere. While thermochemical analysis indicates that carbon exhibits greater susceptibility to oxidation by CO$_2$ compared to metallic iron, experimental data reveal that metallic iron demonstrates a higher oxidation rate than carbon (Figure 5). This discrepancy can be attributed to the predominant existence of fixed carbon located within the benzene ring structure of the reducing agent, where the dissociation of C-O-O-C bonds formed through CO$_2$ adsorption necessitates substantial activation energy [46]. As reported in relevant studies, the gasification reaction of carbon in conventional coal typically initiates at approximately 900 °C, with the gasification rate doubling for every 30 °C to 40 °C increase in temperature [47,48]. Consequently, as depicted in Figure 5a, elevating the oxidation temperature from 900 °C to 1200 °C, the O_{Fe} increases moderately from 88.77% to 95.96%, while the O_C surges from 11.65% to 85.42%.

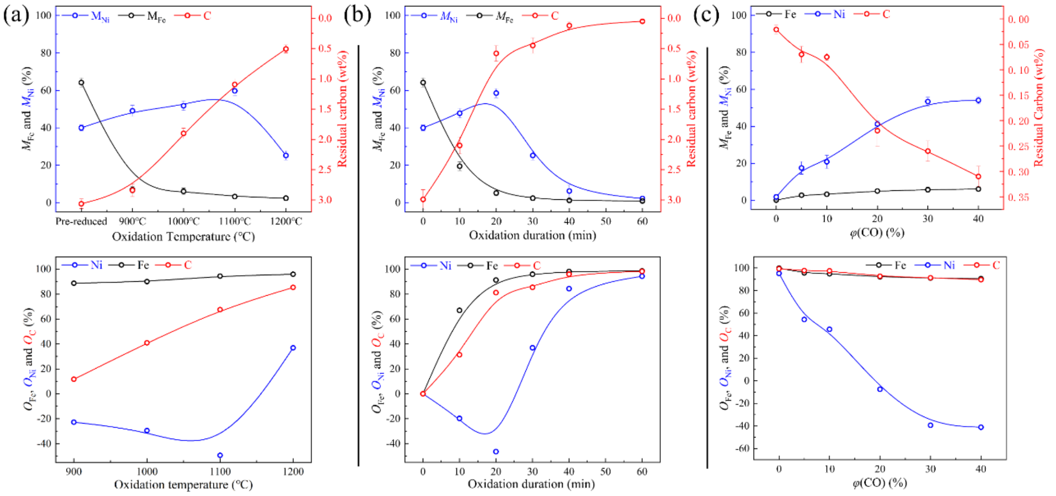

Figure 5. Chemical analysis of oxidized specimens. (a) oxidized for 30 min; (b) oxidized at 1200 °C; (c): oxidized at 1200 °C for 30 min.

In a weakly oxidative atmospheric environment, Fe^{2+} ions, generated through both reduction processes and the oxidation of metallic iron, are expected to continuously diffuse into the silicate matrix without undergoing reduction to metallic iron. The oxidation temperature influences both the stability of Fe^{2+}, as illustrated in Figure 4a, and its diffusion into silicate. As demonstrated in Figures

6a and 7a, at an oxidation temperature of 900 °C, the relatively weak stability of Fe^{2+} coupled with its sluggish diffusion process into the silicate matrix renders Fe^{2+} susceptible to further oxidation. The majority of metallic iron within this oxidized specimen is oxidized into magnetite, thereby forming an iron-rich magnetite-olivine crust covering the silicates. As the oxidation temperature elevated, both the stabilization of Fe^{2+} and their diffusion process enhanced, which consequently inhibits magnetite formation and promotes the formation of iron silicate. From the view of the XRD spectrum (Figure 6a), the magnetite phase is entirely absent at an oxidation temperature of 1100 °C, while the accelerated diffusion kinetics of Fe^{2+} facilitates the homogenization of iron into the silicate matrix, consequently forming silicates of olivine, pigeonite, and enstatite phases. Moreover, microscopic observation indicates that specimens oxidized at 1200 °C exhibit significantly improved sintering characteristics relative to those treated at 900 °C (Figure 8) and exhibit almost complete homogenization of iron within the silicate matrix.

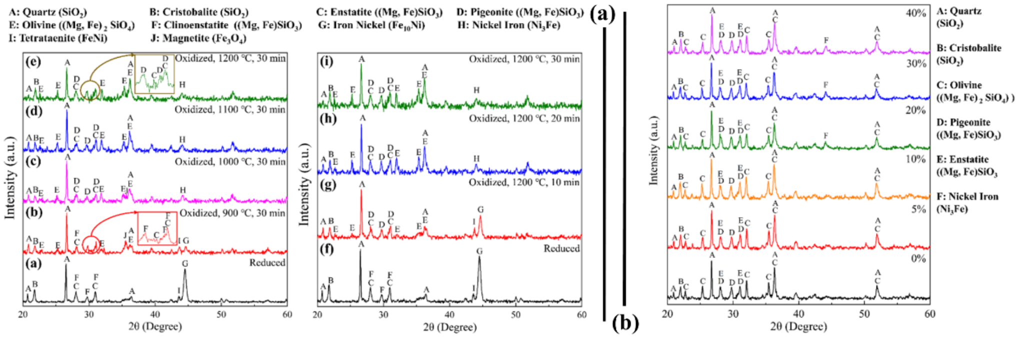

Figure 6. XRD analysis of oxidized specimens. (a) oxidized by pure CO2; (b) oxidized by mixed gases.

Ni^{2+} is more susceptible to the reduction compared to Fe^{2+}, experimental result indicates (Figure 4) a residual carbon content exceeding 0.5 wt% is adequate to maintain a reduction rate of Ni^{2+} that surpasses the oxidation rate of metallic nickel, consequently leading to a progressive increase in M_{Ni} of the specimen. The marked disparity in oxidation resistance between metallic iron and metallic nickel substantially enhances the nickel enrichment within the alloy during the oxidation process. As demonstrated in Figures 7b and 8a, in the specimen oxidized at 900 °C for 30 minutes, nickel displays a nearly identical concentration level to that of iron within the alloy matrix, while exhibits a significantly higher concentration degree within the mineral phase compared to iron. With the elevation of oxidation temperature, the nickel content in the alloy demonstrates progressive enhancement; nevertheless, as the carbon component approaches complete oxidation, the metallic nickel inevitably experiences concurrent oxidation in pure CO_2 environment. Subsequent to a 20-minute oxidation process at 1200 °C, the M_{Ni} of the specimen increased from 40% to 58.5%, whereas the carbon content decreased from 2.99 wt% 0.54 wt%. Further decreased carbon content becomes insufficient to inhibit the oxidation of metallic nickel. Upon extending the oxidation duration to 30 minutes, the M_{Ni} decreased to 25.2%. Concurrently, the oxidation products of metallic nickel diffused into the silicate matrix, exhibiting a similar behavior to that of metallic iron oxidation products (Figure 7b).

From a structural perspective, the iron-nickel alloy exhibits a body-centered cubic lattice configuration, wherein the relatively larger interatomic spacing facilitates oxygen diffusion into the alloy matrix and hinders the tight bonding between oxide films and metal substrates. The oxide film primarily composed of iron oxide exhibits higher propensity for solid-state reactions with silicate matrix compared to nickel oxide. As depicted in Figure 6, iron-nickel alloy presents preferential oxidation to transform into tetrataenite (tetragonal crystal structure) with increased nickel content and denser crystalline arrangement. Following the complete transformation of iron-nickel alloys into tetrataenite, the oxidation rate of iron undergoes a substantial reduction, subsequently leading to a progressive transformation of tetrataenite into a face-centered cubic nickel-iron alloy.

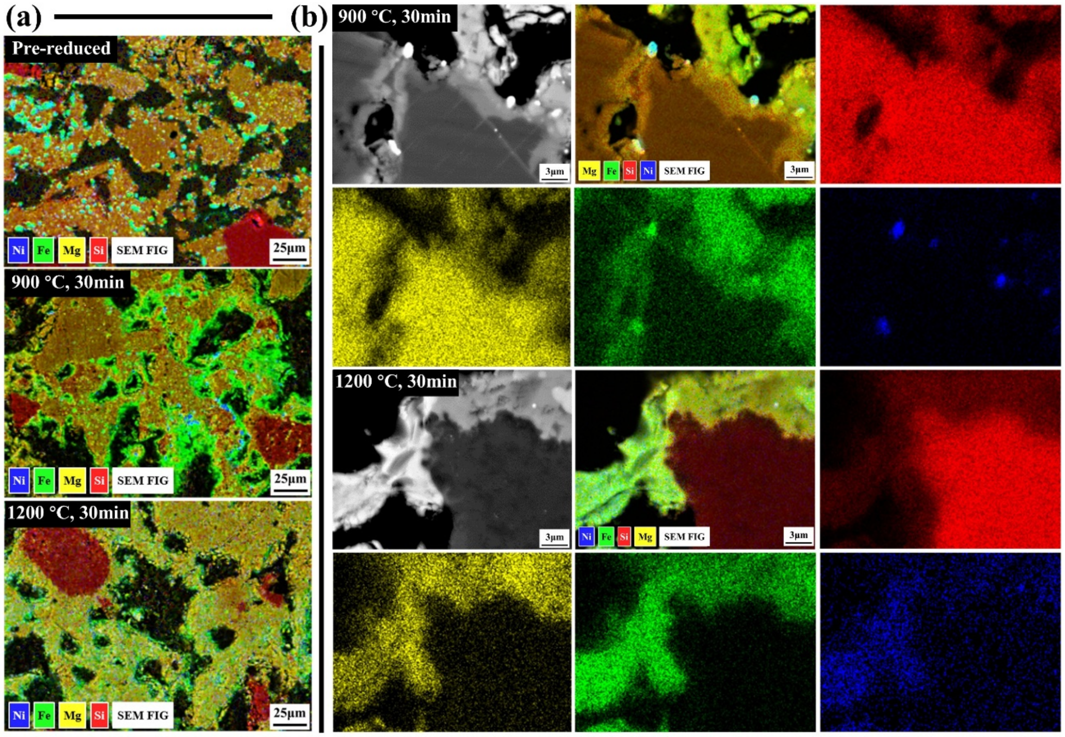

Figure 7. SEM-EDS analysis of cross-sectional surface of specimens oxidized by pure CO_2.

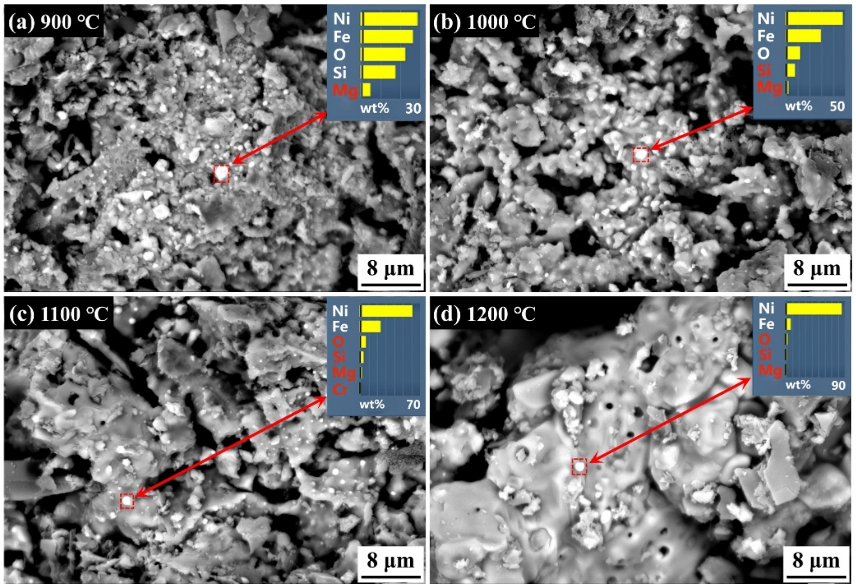

Figure 8. SEM-EDS analysis of fractural surface of specimens oxidized by pure CO_2.

To investigate the effect of CO in oxidation process, a mixed gas atmosphere consisting of CO_2 and CO with a controlled flow rate of 10 L/min was introduced. The entire oxidation process was maintained at 1200 °C for a duration of 30 minutes. As depicted in Figure 5c, the increased gas flow rate markedly accelerated the oxidation rate of the specimens: nearly all metallic nickel, metallic iron, and carbon underwent oxidation in an atmosphere with φ(CO) of 0%. Although CO demonstrates remarkable efficacy in inhibiting the oxidation of metallic nickel, the solid-state interaction between nickel oxidation products and the silicate matrix compromises its reduction kinetics. The experimental findings indicate that the φ(CO) necessary to achieve complete inhibition of metallic nickel oxidation substantially exceeds the thermochemical prediction. In specimens subjected to oxidation in a mixed gas with $\varphi(CO)$ of 5%, a substantial quantity of fine alloy particles is observed, accompanied by a reduction in the O_{Ni} value to 54.3%. However, the residual alloy content remains insufficient to generate distinct diffraction peaks in the XRD spectrum (Figure 6b). Elevating the $\varphi(CO)$ in the gas mixture progressively impairs its oxidative capacity, thereby inhibiting the oxidation of metal, and a corresponding reduction in the nickel content of the alloy (Figure 9a,b). As depicted in Figure 9a, specimen subjected to oxidation under an atmosphere with $\varphi(CO)$ of 30% presents a substantially enhanced nickel concentration and, however, reduced nickel content in the alloy compared to that oxidized at $\varphi(CO)$ of 5%.

Although O_{Ni} transitioned to negative values when $\varphi(CO)$ was increased to 20%, complete inhibition of nickel oxidation required $\varphi(CO)$ to reach approximately 30%. This conclusion can be drawn from two observations: firstly, the O_{Ni} curve (Figure 5b) exhibits a continuous decline when $\varphi(CO)$ reaches 20% but stabilizes when $\varphi(CO)$ approaches 30%. Secondly, upon extending the oxidation duration to 60 minutes, the O_{Ni} in the specimen oxidized at $O_{Ni}(CO)$ of 20% decreased to 17.3%, whereas the specimen oxidized at $O_{Ni}(CO)$ of 30% shows little deviation from its initial value. The negative O_{Ni} value observed in the specimen oxidized at $O_{Ni}(CO)$ of 20% might result from the continuous reduction of Ni^{2+} by residual carbon during the initial oxidation stage, combined with the significantly reduced oxidation rate for metallic nickel in this atmosphere, thereby producing more metallic nickel than was oxidized during the process.

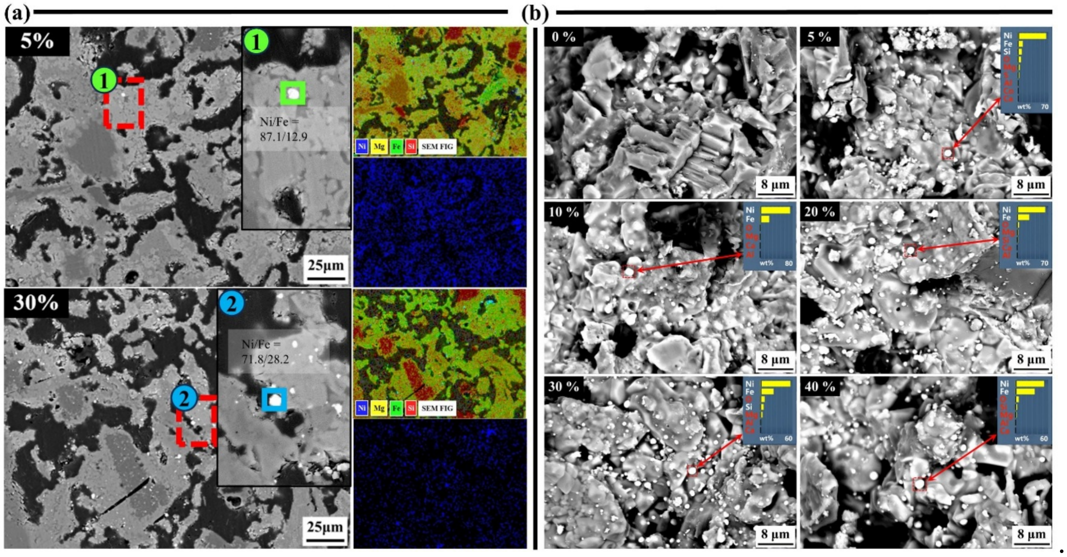

Figure 9. SEM-EDS analysis of specimens oxidized by mixed gas. (a) cross-sectional surface; (b) fractural surface.

3.3. Selective Nickel Reduction

Following the pre-reduction and selective oxidation treatment, Fe(O) homogenizes into the silicate matrix, thereby losing its kinetic advantage for reduction. Given that the primary constituents of the slag generated during the smelting of saprolite-type laterite nickel ore predominantly comprise the $FeO\text{-}MgO\text{-}SiO_2$, its melting point characteristics can be roughly interpreted in Figure 4b. Despite the SiO_2/MgO ratio of the mineral reaching 2.9, the substantial increase in Fe^{2+} content in the silicate matrix during the iron homogenized process significantly reduces the melting point of the slag from about 1800 °C to below 1500 °C. Evidently, the significantly reduced melting point and elevated basicity of slag not only reduce smelting temperature and flux consumption, but also facilitated the metal-slag separation. The experimental results, as illustrated in Figure 10a, demonstrate that during the smelting process of oxidized specimens, the metallization rate of nickel markedly exceeds that of iron: while maintaining R_{Ni} above 95%, R_{Fe} can be less than 10%. Among the smelting products, the highest relative nickel content (*C*(Ni)) in the alloy reaches 85.7%, albeit with a R_{Ni} of only 30.8%. To sustain a R_{Ni} of 95%, specimens oxidized at a φ(CO) of 30% produce alloys with a *C*(Ni) up to 48.2%. Additionally, all oxidized specimens were observed to completely melt below 1500 °C.

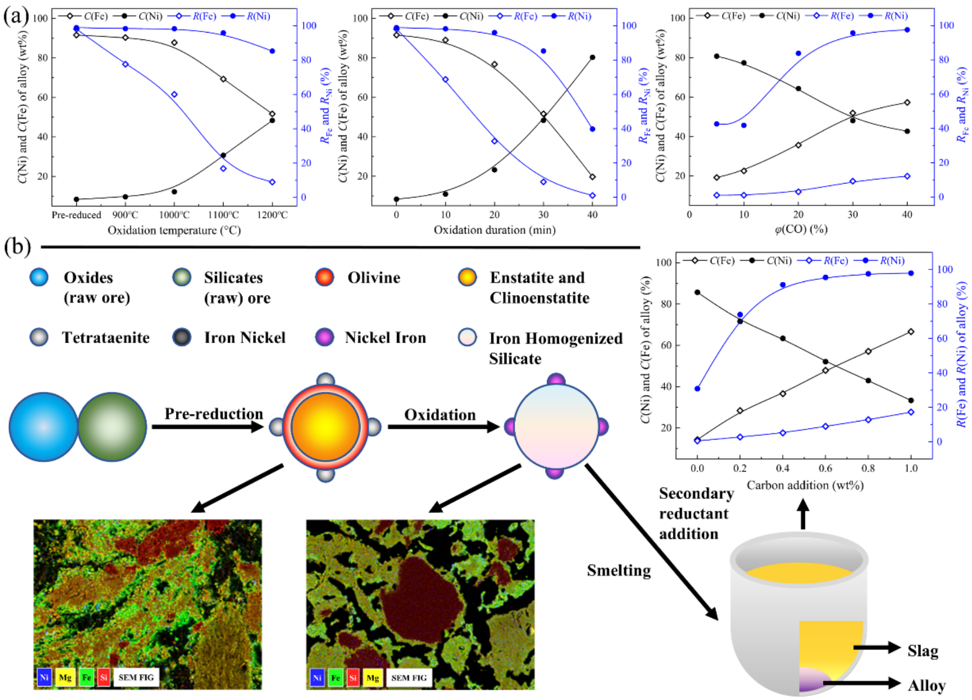

Figure 10. Smelting of the iron homogenized minerals. (a) Alloy produced by smelting oxidized specimens; (b) Optimized process of pre-reduction, CO-CO_2 treatment, and smelting process and the effect of secondary reductant addition to alloy products.

Nevertheless, from both economic and environmental perspectives, excessive reductant usage and over-reduction of minerals would lead to unnecessary energy consumption and increased carbon emissions. From an industrial production standpoint, the selective oxidation process presents challenges in precisely controlling the residual carbon content within the specimen, consequently impeding the accurate regulation of the nickel grade in the alloy. Given that the objective of the pre-reduction and selective oxidation process is to homogenize iron into the silicate phase, following optimizations was implemented: reducing the carbon of the briquette from 6.1wt% to 3.5wt% (equal to 5 wt% anthracite), decreasing the reduction duration to 10 minutes, utilizing gas with φ(CO) of 30% as the oxidation gas, reducing the oxidation duration to 20 minutes, crushing the oxidized specimen and mixing it with the reducing agent prior to smelting, and lowering the smelting temperature to 1550 °C. The schematic representation of this process and the corresponding results are illustrated in Figure 10b. As anticipated, the selective reduction efficacy of nickel maintained exceptional performance following the process optimization: with the incremental addition of carbon from 0 to 0.2 wt% (relative to oxidized mineral), R_{Ni} increases from 30.8% to 70.8%, whereas R_{Fe} merely increases from 0.5% to 2.7%. Notably, the metallization rate of nickel is 18-fold higher than that of iron, with *C*(Ni) in the alloy attains 74.9 wt%. however, the reduction in Ni^{2+} concentration within the slag consequently leads to a decrease in the nickel reduction rate. When the carbon addition reaches 0.4wt% and 0.6 wt%, R_{Ni} achieves 91.2% and 95.5%, while *C*(Ni) of the alloy decreases to 64.2 wt% and 52.1 wt%, respectively. Further augmentation of carbon addition exerts a negligible impact on the enhancement of R_{Ni}, accompanied by a continuous decrease in the nickel grade of the alloy.

It is important to highlight that the oxidized specimens must undergo carbon blending prior to the molten process. As previously mentioned, if the oxidized specimens are subjected to melting initially, followed by carbon spraying onto the slag surface, carbon would concentrate on the slag surface, thereby generating a Ni^{2+} depletion zone surrounding the reductant. Under identical carbon addition of 1.0wt%, the R_{Ni} of the prior carbon blending attains 97.9%, with the C(Ni) in the alloy reaching 33.4%. In contrast, the R_{Ni} and C(Ni) of the alloy in the latter case decrease to 69.4% and 21.8%, respectively.

4. Conclusions

The pre-reduction and CO-CO2 treatment facilitates the migration of iron elements from their original oxide state into silicate structures, thereby achieving compositional homogenization. This process exerts a dual effect: firstly, it compromises the reduction kinetics of the iron within oxides, thereby enhancing the selective reduction of nickel; secondly, it reduces the eutectic point of the mineral matrix to below 1500 °C and elevate the basicity, which is critical for a thorough slag-metal separation, from 0.36 to above 0.8. The combination of pre-reduction process, CO-CO2 treatment, and secondary carbon addition smelting process has demonstrated itself capable to produce a FeNi50 alloy with a nickel content of 52.1 wt% from low-grade laterite nickel ore (characterized by a nickel content of 1.46 wt%, Fe/Ni ratio of 11.3, and SiO2/MgO ratio of 2.9) at a smelting temperature of 1550 °C, with a nickel recovery rate of 95.5% and total carbon consumption of 4wt%. And, if reduced the secondary carbon addition to 0.4 wt% (total carbon consumption of 3.83wt%), the alloy nickel content increased to 64.2 wt% while the nickel recovery rate decreased to 91.2%. This method exhibits potential to enhance the raw material adaptability (expanded Fe/Ni ratio and SiO2/MgO ratio) and selective nickel reduction (6.2-fold nickel concentration of alloy product relative to raw material) in pyrometallurgical process.

Author Contributions: Conceptualization, Zhichao Hu and Guihua Hang.; methodology, Zhichao Hu and Zhengliang Xue.; software, Zhichao Hu.; validation, Zhichao Hu.; formal analysis, Zhichao Hu and Guo Lin.; investigation, Zhichao Hu, Wei Wang, Fang Huang, Yaqi Wang.; resources, Zhengliang Xue.; data curation, Zhichao Hu.; writing—original draft preparation, Zhichao Hu.; writing—review and editing, Zhichao Hu.; visualization, Zhichao Hu.; supervision, Zhengliang Xue. All authors have read and agreed to the published version of the manuscript.

Funding: This research received no external funding.

Conflicts of Interest: The authors declare no conflicts of interest.

References

1. Da, G.; Yang, Z.; Yang, S.; Chen, Y.; Li, Z.; Wang, C.; Xiao, L.; Zhang, Z. Corrosion Behavior of 700 MPa Grade Weathering Steel with 4.0 Wt% Ni and 5.0 Wt% Cr in Simulated Marine Atmospheric Environment. *Construction and Building Materials* **2024**, *414*, 134790, doi:10.1016/j.conbuildmat.2023.134790.
2. Khaleel, A.; Adamson, A.; Pillantakath, A.-R. The Impact of Surface-Impregnated versus Support-Dispersed Fe in Fe–Ni/γ-Al2O3 Catalysts for Partial Oxidation of Methane: Insights into the Effect of Fe Incorporation Method on Coking and on the Reaction Mechanism. *International Journal of Hydrogen Energy* **2024**, *81*, 643–653, doi:10.1016/j.ijhydene.2024.07.191.
3. Liu, W.; Liu, W.; Ji, H.; Tang, X.; Wang, M.; Song, C.; Yang, X. Hot Deformation Behavior and Hot Working Map of Mn–Cr–Ni–Co Steel for Ball Mill Liner Forging Process. *Journal of Materials Research and Technology* **2024**, *30*, 5685–5700, doi:10.1016/j.jmrt.2024.04.182.
4. Liu, X.; Wang, C.; Zhang, Y.; Wang, L.; Xu, W. Design of a 2.7 GPa Ultra-High-Strength High Co–Ni Secondary Hardening Steel by Two-Step Nano-Size Precipitation Tailoring. *Journal of Materials Research and Technology* **2024**, *28*, 4212–4221, doi:10.1016/j.jmrt.2024.01.038.

5. Salehi, H.; Khayyam Nekouei, R.; Maroufi, S.; Sahajwalla, V. Sustainable Recovery of Rare Earth Elements from Ni-MH Batteries: Flux-Free Thermal Isolation and Subsequent Hydrometallurgical Refinement. *Materials Today Sustainability* **2024**, *27*, 100849, doi:10.1016/j.mtsust.2024.100849.
6. Zeng, Y.; Wu, B.; Wang, F. The Effects of Electrolyte Composition and Deposition Voltage on the Copper-Nickel Alloy Micropillars Fabricated by Jet ECD. *Materials Today Communications* **2024**, *40*, 109670, doi:10.1016/j.mtcomm.2024.109670.
7. *Mineral Commodity Summaries 2025*; 1.2.; U.S. Geological Survey, 2025;
8. Dilshara, P.; Abeysinghe, B.; Premasiri, R.; Dushyantha, N.; Ratnayake, N.; Senarath, S.; Sandaruwan Ratnayake, A.; Batapola, N. The Role of Nickel (Ni) as a Critical Metal in Clean Energy Transition: Applications, Global Distribution and Occurrences, Production-Demand and Phytomining. *Journal of Asian Earth Sciences* **2024**, *259*, 105912, doi:10.1016/j.jseaes.2023.105912.
9. Freyssinet, P.; Butt, C.R.M.; Morris, R.C.; Patrice, P. Ore-Forming Processes Related to Lateritic Weathering. *Econ Geol 100th Anniversary* **2005**, 681–722, doi:10.5382/AV100.21.
10. Thorne, R.; Herrington, R.; Roberts, S. Composition and Origin of the Çaldağ Oxide Nickel Laterite, W. Turkey. *Mineralium Deposita* **2009**, *44*, 581–595, doi:10.1007/s00126-009-0234-6.
11. Murofushi, A.; Otake, T.; Sanematsu, K.; Zay Ya, K.; Ito, A.; Kikuchi, R.; Sato, T. Mineralogical Evolution of a Weathering Profile in the Tagaung Taung Ni Laterite Deposit: Significance of Smectite in the Formation of High-Grade Ni Ore in Myanmar. *Miner Deposita* **2022**, *57*, 1107–1122, doi:10.1007/s00126-021-01089-6.
12. Domènech, C.; Galí, S.; Villanova-de-Benavent, C.; Soler, J.M.; Proenza, J.A. Reactive Transport Model of the Formation of Oxide-Type Ni-Laterite Profiles (Punta Gorda, Moa Bay, Cuba). *Miner Deposita* **2017**, *52*, 993–1010, doi:10.1007/s00126-017-0713-0.
13. Thorne, R.; Roberts, S.; Herrington, R. The Formation and Evolution of the Bitincke Nickel Laterite Deposit, Albania. *Mineralium Deposita* **2012**, *47*, 933–947, doi:10.1007/s00126-012-0411-x.
14. Cao, S.; Chang, L.; Bi, X.; Luo, S.; Liu, J. Alkaline Hydrothermal Treatment and Leaching Kinetics of Silicon from Laterite Nickel Ore. *Mining, Metallurgy & Exploration* **2022**, *39*, 129–138, doi:10.1007/s42461-021-00518-4.
15. Dong, B.; Tian, Q.; Xu, Z.; Guo, X.; Wang, Q.; Li, D. The Effect of Pre-Roasting on Atmospheric Sulfuric Acid Leaching of Saprolitic Laterites. *Hydrometallurgy* **2023**, *218*, 106063, doi:10.1016/j.hydromet.2023.106063.
16. Ribeiro, P.P.M.; De Souza, L.C.M.; Neumann, R.; Dos Santos, I.D.; Dutra, A.J.B. Nickel and Cobalt Losses from Laterite Ore after the Sulfation-Roasting-Leaching Processing. *Journal of Materials Research and Technology* **2020**, *9*, 12404–12415, doi:10.1016/j.jmrt.2020.08.082.
17. Zhai, X.; Fu, Y.; Zhang, X.; Ma, L.; Xie, F. Intensification of Sulphation and Pressure Acid Leaching of Nickel Laterite by Microwave Radiation. *Hydrometallurgy* **2009**, *99*, 189–193, doi:10.1016/j.hydromet.2009.08.006.
18. He, F.; Ma, B.; Qiu, Z.; Wang, C.; Chen, Y.; Hu, X. Enhanced Extraction of Nickel from Limonitic Laterite via Improved Nitric Acid Pressure Leaching Process. *Minerals Engineering* **2023**, *201*, 108170, doi:10.1016/j.mineng.2023.108170.
19. Zhang, P.; Sun, L.; Wang, H.; Cui, J.; Hao, J. Surfactant-Assistant Atmospheric Acid Leaching of Laterite Ore for the Improvement of Leaching Efficiency of Nickel and Cobalt. *Journal of Cleaner Production* **2019**, *228*, 1–7, doi:10.1016/j.jclepro.2019.04.305.
20. Faris, N.; Fischmann, A.J.; Assmann, S.; Jones, L.A.; Tardio, J.; Madapusi, S.; Grocott, S.; Bhargava, S. A Study into the Behaviour of Nickel, Cobalt and Metal Impurities during Partial Neutralisation of Synthetic Nickel Laterite Pressure Leach Solutions and Pulps. *Hydrometallurgy* **2021**, *202*, 105604, doi:10.1016/j.hydromet.2021.105604.
21. Faris, N.; White, J.; Magazowski, F.; Fischmann, A.; Jones, L.A.; Tardio, J.; Madapusi, S.; Grocott, S.; Bhargava, S.K. An Investigation into Potential Pathways for Nickel and Cobalt Loss during Impurity Removal from Synthetic Nickel Laterite Pressure Acid Leach Solutions via Partial Neutralisation. *Hydrometallurgy* **2021**, *202*, 105595, doi:10.1016/j.hydromet.2021.105595.
22. Mang, C.; Li, G.; Chen, Y.; Luo, J.; Rao, M.; Jiang, T. Efficient Removal of Iron during Partial Neutralization of Nickel Laterite Acid Leach Solution: DFT Calculation and Experimental Verification of Mechanism. *Hydrometallurgy* **2023**, *220*, 106090, doi:10.1016/j.hydromet.2023.106090.

23. Asadrokht, M.; Zakeri, A. Chemo-Physical Concentration of a Low-Grade Nickel Laterite Ore. *Minerals Engineering* **2022**, *178*, 107398, doi:10.1016/j.mineng.2022.107398.
24. Borda, J.; Torres, R. Effect of Pretreatments to Improve Nickel Leaching from Laterites in Carboxylic Media: Mechanism and Kinetic Model. *South African Journal of Chemical Engineering* **2023**, *46*, 12–21, doi:10.1016/j.sajce.2023.07.001.
25. Mohammadreza, F.; Mohammad, N.; Ziaeddin, S.S. Nickel Extraction from Low Grade Laterite by Agitation Leaching at Atmospheric Pressure. *International Journal of Mining Science and Technology* **2014**, *24*, 543–548, doi:10.1016/j.ijmst.2014.05.019.
26. Sakamoto, T.; Hanada, T.; Sato, H.; Kamisono, M.; Goto, M. Hydrophobic Deep Eutectic Solvents for the Direct Leaching of Nickel Laterite Ores: Selectivity and Reusability Investigations. *Separation and Purification Technology* **2024**, *331*, 125619, doi:10.1016/j.seppur.2023.125619.
27. Zhai, Y.; Mu, W.; Liu, Y.; Xu, Q. A Green Process for Recovering Nickel from Nickeliferous Laterite Ores. *Transactions of Nonferrous Metals Society of China* **2010**, *20*, s65–s70, doi:10.1016/S1003-6326(10)60014-3.
28. Hu, Z.; Wang, J.; Xue, Z.; Wang, W.; Huang, F.; Mei, X. The Carbothermic Reduction Behaviour of Saprolitic Laterite Nickel Ore and the Enhancement Mechanisms of Selective Nickel Reduction Induced by CaO and CaF2 Incorporation. *Journal of Materials Research and Technology* **2025**, *38*, 392–405, doi:10.1016/j.jmrt.2025.07.217.
29. Ma, B.; Li, X.; Yang, W.; Hu, D.; Xing, P.; Liu, B.; Wang, C. Nonmolten State Metalized Reduction of Saprolitic Laterite Ores: Effective Extraction and Process Optimization of Nickel and Iron. *Journal of Cleaner Production* **2020**, *256*, 120415, doi:10.1016/j.jclepro.2020.120415.
30. Farrokhpay, S.; Filippov, L.; Fornasiero, D. Pre-Concentration of Nickel in Laterite Ores Using Physical Separation Methods. *Minerals Engineering* **2019**, *141*, 105892, doi:10.1016/j.mineng.2019.105892.
31. Zhang, Z.; Zhang, W.; Zhang, Z.; Chen, X.; Development Research Center of China Geological Survey, Ministry of Natural Resources, Beijing 100037, China; Inner Mongolia University of Technology, Hohhot 010062, China Nickel Extraction from Nickel Laterites: Processes, Resources, Environment and Cost. *China Geology* **2024**, *7*, 1–27, doi:10.31035/cg2024124.
32. Eckelman, M.J. Facility-Level Energy and Greenhouse Gas Life-Cycle Assessment of the Global Nickel Industry. *Resources, Conservation and Recycling* **2010**, *54*, 256–266, doi:10.1016/j.resconrec.2009.08.008.
33. Jiang, M.; Sun, T.; Liu, Z.; Kou, J.; Liu, N.; Zhang, S. Mechanism of Sodium Sulfate in Promoting Selective Reduction of Nickel Laterite Ore during Reduction Roasting Process. *International Journal of Mineral Processing* **2013**, *123*, 32–38, doi:10.1016/j.minpro.2013.04.005.
34. Li, G.; Shi, T.; Rao, M.; Jiang, T.; Zhang, Y. Beneficiation of Nickeliferous Laterite by Reduction Roasting in the Presence of Sodium Sulfate. *Minerals Engineering* **2012**, *32*, 19–26, doi:10.1016/j.mineng.2012.03.012.
35. Zhu, D.Q.; Cui, Y.; Vining, K.; Hapugoda, S.; Douglas, J.; Pan, J.; Zheng, G.L. Upgrading Low Nickel Content Laterite Ores Using Selective Reduction Followed by Magnetic Separation. *International Journal of Mineral Processing* **2012**, *106–109*, 1–7, doi:10.1016/j.minpro.2012.01.003.
36. Zhu, D.; Pan, L.; Guo, Z.; Pan, J.; Zhang, F. Utilization of Limonitic Nickel Laterite to Produce Ferronickel Concentrate by the Selective Reduction-Magnetic Separation Process. *Advanced Powder Technology* **2019**, *30*, 451–460, doi:10.1016/j.apt.2018.11.024.
37. Manzoor, U.; Mujica Roncery, L.; Raabe, D.; Souza Filho, I.R. Sustainable Nickel Enabled by Hydrogen-Based Reduction. *Nature* **2025**, *641*, 365–373, doi:10.1038/s41586-025-08901-7.
38. Zulhan, Z.; Shalat, W. Evolution of Ferronickel Particles during the Reduction of Low-Grade Saprolitic Laterite Nickel Ore by Coal in the Temperature Range of 900–1250 °C with the Addition of CaO-CaF2-H3BO3. *Int J Miner Metall Mater* **2021**, *28*, 612–620, doi:10.1007/s12613-020-2025-0.
39. Wang, X.; Sun, T.; Chen, C.; Kou, J. Effects of Na2SO4 on Iron and Nickel Reduction in a High-Iron and Low-Nickel Laterite Ore. *Int J Miner Metall Mater* **2018**, *25*, 383–390, doi:10.1007/s12613-018-1582-y.
40. Hang, G.; Xue, Z.; Wu, Y. Preparation of High-Grade Ferronickel from Low-Grade Nickel Laterite by Self-Reduction and Selective Oxidation with CO2-CO Gas. *Minerals Engineering* **2020**, *151*, 106318, doi:10.1016/j.mineng.2020.106318.

41. Sun, N.; Wang, Z.; Guo, Z.; Zhang, G.; Qi, T. Effects of Temperature, CO Content, and Reduction Time on the Selective Reduction of a Limonitic Laterite Ore. *Minerals Engineering* **2021**, *174*, 107277, doi:10.1016/j.mineng.2021.107277.
42. Li, Z.; Qi, H.; Fu, Z.; Cui, H.; Xiao, P.; Yang, L. Separation Methods of Nickel in Different Phases of Laterite Nickel Ore 2023.
43. Wang, H.; Wei, Y.; Li, B.; Hu, J.; Wang, W.; Chen, G. A Method for the Determination of Metallic Nickel in the Reduction Product of Laterite Nickel Ore 2011.
44. Ponomar, V.P.; Brik, O.B.; Cherevko, Yu.I.; Ovsienko, V.V. Kinetics of Hematite to Magnetite Transformation by Gaseous Reduction at Low Concentration of Carbon Monoxide. *Chemical Engineering Research and Design* **2019**, *148*, 393–402, doi:10.1016/j.cherd.2019.06.019.
45. Xu, C.; Sun, T.; Kou, J.; Li, Y.; Mo, X.; Tang, L. Mechanism of Phosphorus Removal in Beneficiation of High Phosphorous Oolitic Hematite by Direct Reduction Roasting with Dephosphorization Agent. *Transactions of Nonferrous Metals Society of China* **2012**, *22*, 2806–2812, doi:10.1016/S1003-6326(11)61536-7.
46. Luo, H.; Wang, Y.; Xuan, W.; Zhang, J. Study on CO2 Gasification Mechanism of Bituminous Coal Coke by In-Situ Measurement and DFT Calculation. *Surfaces and Interfaces* **2025**, *66*, 106560, doi:10.1016/j.surfin.2025.106560.
47. You, Z.; Chen, K.; Xiao, J.; Mao, Q.; Zhong, Q.; Wang, X.; Li, J. Bidirectional Regulation on CO2 Gasification of Coke by Trace Native Impurities: Catalytic Effect Quantification and Atomic Mechanism. **2025**.
48. Xu, J.; Zuo, H.; Wang, G.; Zhang, J.; Guo, K.; Liang, W. Gasification Mechanism and Kinetics Analysis of Coke Using Distributed Activation Energy Model (DAEM). *Applied Thermal Engineering* **2019**, *152*, 605–614, doi:10.1016/j.applthermaleng.2019.02.104.